Bani Asadi, Hossein; Seppälä, Jukka

Novel long-chain aliphatic polyamide/surface-modified silicon dioxide nanocomposites: in-situ polymerization and properties

Published in:
Materials Today Chemistry

DOI:
10.1016/j.mtchem.2021.100450

Published: 01/06/2021

Document Version
Publisher's PDF, also known as Version of record

Materials Today Chemistry 20 (2021) 100450

Contents lists available at ScienceDirect

Materials Today Chemistry

journal homepage: www.journals.elsevier.com/materials-today-chemistry/

Novel long-chain aliphatic polyamide/surface-modified silicon dioxide nanocomposites: *in-situ* polymerization and properties

H. Baniasadi, J. Seppälä*

Polymer Technology, School of Chemical Engineering, Aalto University, Espoo, Finland

ARTICLE INFO

Article history:
Received 8 December 2020
Received in revised form
9 February 2021
Accepted 11 February 2021
Available online 13 March 2021

Keywords:
Long-chain aliphatic polyamide
Surface modification
Silicon dioxide

ABSTRACT

A new kind of long-chain aliphatic polyamide (PA1218) with a relatively low melting point, high molecular weight, and stable mechanical properties at humid conditions was successfully developed via a polycondensation reaction between 1,18-octadecanedioic acid and 1,12-diaminodecane. Additionally, oleic acid-surfaced modified silicon dioxide (SSD) was prepared and employed to improve the properties of PA1218 through *in-situ* polymerization. FT-IR spectra and TGA thermograms confirmed the successful surface modification of nanoparticles, and consequently, 5% substitution of surface hydroxyl groups of SiO_2 nanoparticles with oleic acid molecules. Moreover, the thermomechanical and rheology tests revealed a significant improvement in nanocomposites' properties compared to the pure PA1218; for instance, the tensile strength and storage modulus were increased by 22% and 40%, respectively in the sample containing 3% SSD nanoparticles. This improvement, along with SEM images, confirmed the uniform dispersion of SSD nanoparticles through the employed *in-situ* polymerization and excellent compatibility between inorganic and organic phases, which was achieved via surface modification. Finally, all the samples demonstrated a water uptake capacity of less than 0.6% attributed to the high methylene/amide ratio in their backbones, causing these newly developed nanocomposites to be notable candidates for specific engineering applications.

1. Introduction

Linear aliphatic polyamides (PAs) are versatile engineering thermoplastics produced in large quantities for decades. They comprise the right balance of properties, including significant resistance to wear and abrasion, considerable mechanical properties even at elevated temperatures, low permeability against gases, good chemical resistance, and dimensional stability owing to the strong intermolecular and intramolecular hydrogen bonds between the amide groups [1–4]. However, due to the amide moiety, they are water-sensitive, requiring an efficient drying process. The sorption of water molecules lowers the glass transition temperature due to the plasticization of the amorphous regions of partially crystalline polymeric systems and consequently reduces the mechanical properties. An increase in the length of aliphatic sequences could be an excellent solution to address this drawback since there is a probable tendency that PA performs more like polyethylene if the density of amide groups (−NHCO−) along molecular chains becomes very low [3,5–7]. As a result, studies on long alkane segment PAs have attracted much attention in recent years. Specific long-chain aliphatic PAs, which possess a repeating unit with a 20 or higher carbon number, have been well developed in the last decade. These long repeating units, which can be derived from the dicarboxylic acid segment (e.g., PA614, PA616, PA618) or the diamine component (e.g., PA1010, PA1016, and PA1216), have a higher ratio of methylene: amide linkages per repeating units. Therefore, they adsorb lower moisture, giving these PAs a competitive edge over the shorter-chain ones, such as PA6 and PA66. For this purpose, they have found use in a broad field of applications, such as packaging, automotive components, sporting equipment, cables, and tubing [6,8].

Furthermore, organic-inorganic nanocomposites regarded as innovative advanced materials have gained increasing attention in the field of materials science and engineering. They have the desirable properties of a ceramic phase, such as heat resistance, retention of mechanical properties at elevated temperatures, and low thermal expansion, and those of organic polymers, including toughness, ductility, and processability [9,10]. These engineered materials could be called nanocomposites if at least one dimension

* Corresponding author.
E-mail address: jukka.seppala@aalto.fi (J. Seppälä).

https://doi.org/10.1016/j.mtchem.2021.100450

of the inorganic phase is below 100 nm [10,11]. It is known that the properties of the resulting nanocomposites strongly depend on the characteristics, dimensions, and shapes of inorganic fillers and their dispersion, as well as compatibility with the organic phase [12,13]. Incorporating well-dispersed silica, which exhibits chemical inertness, nontoxicity, optical transparency, and excellent thermal stability and hardness, can improve the thermal and mechanical properties of PAs [14,15]. However, the untreated silica nanoparticles have poor dispersibility in the PA matrix even at low concentrations due to the hydrogen bonds between vicinal silanol groups of silica; therefore, the final composite properties may decrease even lower than the primary polymer may do. Surface modification is one of the efficient solutions to address this drawback; accordingly, amino-functionalized silica [16],x carboxylated silica [17], fluorinated silica [18], and phosphorylated silica [19] have been developed. Furthermore, among the well-known methods employed to prepare nanocomposites, such as sol-gel processing, solution casting, melt blending, and *in-situ* polymerization, the latter has shown considerable potential to overcome the aggregation tendency of nanoparticles in the polymer matrix [20,21].

In the current study, a new type of long-chain aliphatic polyamide 1218 (PA1218) and its nanocomposite with surface-modified silicon dioxide (SSD) were developed through *in-situ* polymerization. The remarkable thermomechanical properties of the prepared samples and the improved hydrophobicity have made them an exciting candidate for a wide range of engineering applications.

2. Experimental

2.1. Materials

1,18-Octadecanedioic acid (ODA) was purchased from Cathay Biotech Company, China. Silicon dioxide nanopowder (10–20 nm particle size) and sodium hypophosphite monohydrate (≥99%) were obtained from Sigma. 1,12-diaminodecane (≥98%) was purchased from TCI, Japan. Oleic acid (technical grade, ≥90%) and n-hexane (99%) were supplied from Alfa Aesar. Laboratory grade ethanol (92.4%, ETAX B) was supplied from ALTIA Industrial, Finland.

2.2. Preparation of oleic acid surface-modified silica nanoparticles

SiO_2 nanoparticles' surface was modified with oleic acid (OA) molecules through a reaction between OA's carboxylic acid groups and the hydroxyl groups of SiO_2 [17,22]. Initially, 1.0 g of SiO_2 nanoparticles were dispersed in 100 mL n-hexane by 30 min ultrasonication. Then, 1.0 g of OA was added to the mixture, while the system was stirred at 80 °C. The mixing was continued for 4 h at 80 °C, followed by another 1 h in the ice bath. Afterward, the mixture was centrifuged and washed several times with ethanol/water solution (70/30) before drying at −40 °C. The final white powder, which was OA surface-modified silica nanoparticles, was coded as SSD and employed to prepare nanocomposites.

2.3. Synthesis of polyamide 1218 and nanocomposites

PA1218 was synthesized with the method developed in our previous works with significant modifications [6,23]. An identical mole of C12 and C18 as monomers was added to the high-torque reactor equipped with a heating jacket and an overhead mixer. The temperature was gradually increased to 210 °C, and the reaction was continued for 4 h under nitrogen flow and mild stirring. The final product was removed by cooling the reactor, while the system was kept under nitrogen flow to avoid any oxidation. Then, it was milled using the Retsch SM 300 Cutting Mill at 1000 RPM with a blade size of 1 mm and finally hot-pressed (200 C, 150 kPa) to prepare film shape samples for further characterizations. For synthesizing PA1218/SSD, a prescribed amount of SSD was dispersed in ethanol through 30 min sonication, and then ODA was added, and the system was mixed for 1 h. Afterward, the mixture was dried overnight at ambient temperature. The dried ODA/SSD was employed to synthesize the PA1218/SSD nanocomposite with a similar method previously described for the pure polymer. The SSD amount into the matrix was selected as 1, 3, and 5%, and the samples were coded as PA-SSD1, PA-SSD3, and PA-SSD5, respectively. It is noteworthy that the most published PA/silica nanocomposite materials contain similar amounts of filler since higher loading often results in a decrease in mechanical properties like tensile strength [24].

2.4. Characterization

2.4.1. Fourier transform infrared spectroscopy

FT-IR measurement was performed on a PerkinElmer FT-IR Labsence model with an ATR instrument (USA) in a reflection mode. The spectra were obtained by accumulating 32 scans in the wavenumber range of 4000–500 cm^{-1} at the resolution of 4 cm^{-1}.

2.4.2. X-ray diffraction

XRD measurements were performed on PANalytical X'Pert Pro model MPD Alpha 1 (Netherland). The sample was scanned from 5 to 30° at a scan rate of 5°.min^{-1} (Cu Kα radiation, $\lambda = 0.1542$ nm, voltage 40 kV, current 50 mA).

2.4.3. Proton nuclear magnetic resonance spectroscopy

^{1}H NMR measurements were performed with a Bruker NMR Spectrometer model Avance III 400 (USA) operating at 400 MHz (9.4 T). Chloroform-d1 (deuteration at no less than 99.8%) with 10% v/v trifluoroacetic anhydride was utilized as the solvent. The test was conducted at room temperature.

2.4.4. Gel Permeation Chromatography

GPC was conducted with a Waters Whyatt Malls model 717 plus Autosampler (USA) in chloroform-d1 with a 10% v/v trifluoroacetic anhydride solvent at 25 °C. A series of polystyrene standards were used for column calibration.

2.4.5. Scanning electron microscopy

SEM images were taken from the sample's cross-section area after sputtering with gold using the Zeiss Instrument model Sigma VP (Germany) at the voltage of 10 kV with different magnifications. Furthermore, the SSD morphology was studied with an SEM image.

2.4.6. Water absorption

All the samples' water absorption capacity was measured by monitoring the already-dried sample's weight changes (m_0) soaked in the distilled water at 25 °C after 48 h. The sample was taken out, and excess water was dried gently from its surface with tissue paper and immediately weighted (m_w). The water absorption percentage (WA%) was calculated using Eq. (1). Each measurement was repeated three times, and the average value ± error of the mean was reported.

$$WA\ (\%) = \frac{m_w - m_0}{m_0} \times 100 \quad (1)$$

2.4.7. Tensile test

The tensile test was conducted using an Instron Universal Tensile Tester model 4204 (USA) based on ASTM D882 with a 2 kN static load cell. The measurements were strain-control with an increasing strain rate of 10 mm/min. The dog bone shape specimen was allowed to equilibrate in a humidity-controlled atmosphere (50%) at 25 °C for 48 h before the test. For the pure PA1218, the measurement was also performed in a dried condition in which the sample was dried at a vacuum oven 48 h before the measurement to investigate the effect of water absorption on the mechanical properties of the matrix. The Young's modulus, yield strength, tensile strength, elongation at break, and toughness calculating from the stress-strain curve's surface area up to the maximum extension, were determined. The presented results were the average of three reproducible repeats ± standard error of the mean.

2.4.8. Dynamic mechanical analysis

DMA was carried out using a TA Instruments model Q800 (USA) in tension film mode in the temperature range of 25–175 °C with a heating rate of 5 °C/min, at a frequency of 1 Hz, strain of 1%, and pre-load of 1 N. The storage modulus (E′), loss modulus (E″), and loss tangent (tan δ) were measured as a function of temperature for all the samples under identical conditions.

2.4.9. Differential Scanning Calorimetry

DSC was performed on a TA-Instruments model MT-DSC Q2000 (USA) equipped with a cooling system under the nitrogen atmosphere. Two heating-cooling cycles in the range of −20 to 250 °C were applied with a 10 °C/min scan rate. The crystallization temperature (T_c), melting temperature (T_m), crystallization enthalpy (ΔH_c), and melting enthalpy (ΔH_m) were determined from the second cycle. The degree of crystallinity (χ_c) was calculated using Eq. (2) in which ΔH_c was cold crystallization (zero in this study), and ΔH_m^0 was the melting enthalpy of a 100% crystalline specimen. To the best of the authors' knowledge, there is no reported value for 100% crystalline PA1218; therefore, the value of purely crystalline PA1212 (292.2 J/g) was used since it had the closest structural counterpart to the aforementioned synthesized polyamide [25].

$$X_c = \frac{\Delta H_m - \Delta H_c}{\Delta H_m^0} \times 100 \quad (2)$$

2.4.10. Thermal gravimetric analysis

TGA was performed with a TA Instruments model Q500 (USA) under nitrogen flow with a heating rate of 10 °C/min from 30 to 700 °C to investigate the thermal stability of the samples. Furthermore, the amount of a substituted OA on the surface of nanoparticles was measured by comparing the TGA thermograms of SiO_2 before and after surface modification.

2.4.11. Rheological measurements

The melt state's dynamic rheological measurements were performed using an Anton Paar model Physica MCR 301 (Austria) rotational rheometer at 190 °C under a nitrogen atmosphere. The rheological properties of the samples, including storage modulus (G′), loss modulus (G″), complex viscosity (|η*|), and loss factor, were measured in oscillatory shear mode using 25 mm-diameter parallel plates at a gap of 1 mm. The above-mentioned properties were recorded as a function of angular frequency in the range from 0.01 to 100 Hz at a fixed strain of 5%.

3. Results and discussion

3.1. Characterization of oleic acid-surface modified silica nanoparticles

Fig. 1a depicts the FT-IR spectra of SiO_2, SSD, and OA. Although the characteristic peak at 1720 cm^{-1} originated from −COOH groups of OA disappeared in SSD, the peak at 3410 cm^{-1} belonging to −OH groups of silicon dioxide became weak. Additionally, three new peaks appeared in the spectra of SSD at 2940, 2856, and 1462 cm^{-1}, which corresponded to the absorptions of the $-CH_2$ asymmetrical stretching, symmetrical stretching, and scissoring vibrations, which originated from OA, respectively [17,22]. Overall, the FT-IR spectra could confirm the successful surface modification of SiO_2 nanoparticles with OA through a reaction between the carboxylic acid and the Si−OH groups.

To investigate the amount of grafted OA on the surface of SiO_2 nanoparticles, TGA was performed on the pure SiO_2 and SSD (Fig. 1b). There were significant differences between the thermograms of unmodified and modified nanoparticles; the SiO_2 illustrated a low weight loss up to 700 °C owing to dehydration of surface hydroxyl groups [26] without any peak in the DTG curve (Fig. S1). In comparison, SSD revealed a higher weight loss with a DTG peak at 345 °C due to the degradation of organic compounds grafted on the surface of SiO_2. Although SiO_2 exhibited a weight loss of 7.5% after heating up to 700 °C, SSD nanoparticles revealed 12.5%, indicating a successful grafting of 5% of OA on the surface of SiO_2 via the reaction between Si−OH and −COOH groups [26,27]. The grafted OA percentage was also measured by the elemental analysis (Thermo Flash Smart CHNSO Elemental Analyzer). The amounts of carbon were 0.0243% and 5.2226%for the pure SiO_2 and SSD, respectively, indicating a successful grafting of approximately 5.2% OA on the surface of silica nanoparticles.

The morphology of the surface-modified silica nanoparticles was investigated using SEM images. The surface-modified nanoparticles demonstrated spherical clusters with an average diameter of 60 ± 20 nm (Fig. 1c), confirming that the surface treatment did not significantly affect the SiO_2 morphology (spherical nanoparticles with the particle size of 10–20 nm, Fig. S2). Furthermore, SSD illustrated a broad peak centered at 22° (Fig. 1d), assigned to the amorphous characteristic of SiO_2 [28], indicating that the surface modification did not change the silicon dioxide structure.

3.2. Chemical and morphological studies of the synthesized polyamide 1218 and nanocomposites

Fig. 2 presents the FT-IR and ^1H NMR spectra of the synthesized PA1218. The FT-IR spectrum of PA1218 (Fig. 2a) demonstrated a peak at 3305 cm^{-1} assigned to the N−H stretching, and two sharp absorption peaks at 2917 and 2849 cm^{-1} corresponded to the methylene stretching vibration. Furthermore, it exhibited several sharp absorption peaks at around 1634, 1537, 1467, 1256, and 681 cm^{-1} assigned to amide-I (C═O stretching vibration), amide-II (C−N stretching and N−H bending vibration), amide-III (C−H in-of-plane bending vibration), amide-IV (C−CO stretching vibration) and amide-V (N−H out-of-plane bending vibration), respectively. The appeared peaks were in good agreement with other scientific literature [2,29]. These peaks were repeated in all PA-SSD nanocomposites (Fig. S3) with slight displacement. Furthermore, a new peak appeared for all the nanocomposite samples at 1107 cm^{-1}, attributed to the presence of SSD in the nanocomposite. The successful synthesis of PA1218 was more investigated via ^1H NMR spectra (Fig. 2b), where two signals appeared in the region around 3.7 and 2.8 ppm (peaks a and b, respectively) assigned to the methylene proton adjacent to the amino group (CH_2−NH-) and a

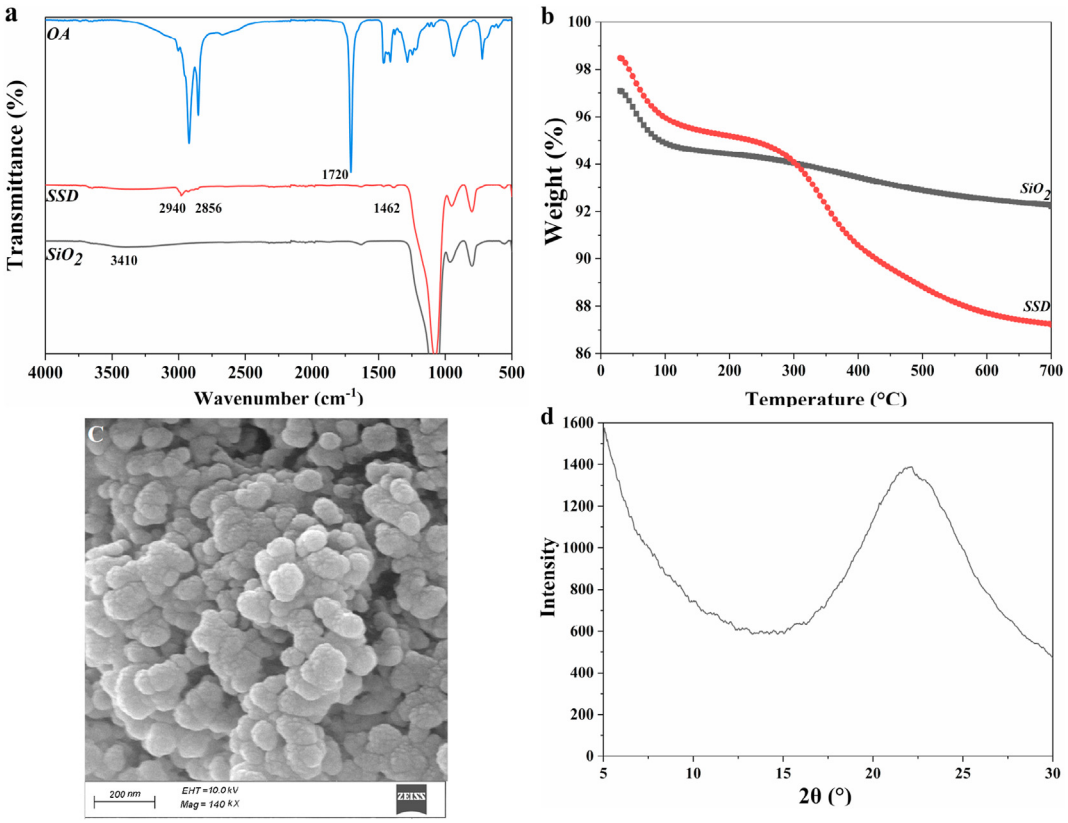

Fig. 1. a) FT-IR spectra of SiO_2, SSD, and OA. (b) TGA thermograms of SiO_2 and SSD. (c) SEM image of SSD nanoparticles with 140 kx magnification. (d) XRD pattern of SSD nanoparticles.

carbonyl group (−CO−CH_2), respectively. Moreover, the peaks at 1.6 and 1.3 ppm correlated with protons along the aliphatic chain [6,8]. To sum up, the FT-IR results, along with the ^{1}H NMR spectrum, could confirm the successful synthesis of PA1218 via a reaction between ODA and diaminodecane.

The number average molecular weight (Mn), weight average molecular weight (Mw), and polydispersity index of the synthesized PA1218 were 87,900 g/mol, 157,500 g/mol, and 1.79, respectively (Fig. S4). The novel synthesized PA1218 revealed relatively higher molecular weight than the short-chain and long-chain PAs did [6,30]. It could be attributed to effective water removal, and the mechanical agitation during the polycondensation reaction encouraged chain growth and reduced the likelihood of chain scission (degradation) or reaction termination [6]. Furthermore, the precise stoichiometric amount of the fed monomers with relatively high molecular weight could be another reason for observing such great molecular weight.

The dispersion of SSD into the PA1218 matrix and the compatibility between inorganic and organic phases were investigated using SEM images (Fig. 2c and d). The SSD nanoparticles were uniformly distributed into the PA1218 matrix via the employed *in-situ* polymerization (Fig. 2c). Furthermore, no apparent segregation of SSD and the formation of any voids around nanoparticles in any region across the films could be detected, demonstrated good compatibility between inorganic and organic phases due to the successful surface modification of nanoparticles with OA. For supporting the positive impact of surface modification on the compatibility between organic and inorganic phases, the SEM image was taken from the cross-section area of the nanocomposite prepared by 3 wt% unmodified silica nanoparticles (Fig. 2d). As illustrated, the nanoparticles were heterogeneously distributed in the polymer matrix and agglomerated to each other, being attributed to the very high tendency of silica nanoparticles to adhere to each other, as reported in the specific scientific literature [10,24].

3.3. Crystallization behavior of the synthesized polyamide 1218 and nanocomposites

The crystal structure of PA1218 and PA-SSD nanocomposites were studied with XRD and DSC analyses (Fig. 3). PA as a polymorphic material can crystallize in two major phases; γ- and α-crystalline forms. The former is more thermodynamically stable and consists of antiparallel molecules in an extended zigzag chain conformation with the ethylene segment and amide group in the same plane, while the latter form is less stable with the hydrogen bonding almost perpendicular to the carbon plane and between parallel chains. It has been known that the α-crystalline phase consists mainly of two characteristic diffraction peaks at approximately 20° and 24°, and the γ-crystalline phase consists mainly of one characteristic diffraction peak at approximately 22° [31,32]. As provided in Fig. 3a, the synthesized PA1218 demonstrated a sharp peak at approximately 20° attributed to the inter-chain distance of the α-crystalline phase, with a shoulder at approximately 22° suggesting the presence of the γ-crystalline structure [3]. These two peaks were repeated in all the nanocomposite samples, which could confirm that the presence of SSD nanoparticles did not make any new crystalline phase in the PA1218 matrix. Furthermore, the SSD diffraction peak at 22° (Fig. 1d) could not be detected in all the nanocomposite, probably due to its overlapping with the more substantial peak attributed to the γ-crystalline phase.

The melting and crystallization behavior of neat PA1218 and PA-SSD nanocomposites was investigated by cyclic DSC measurements.

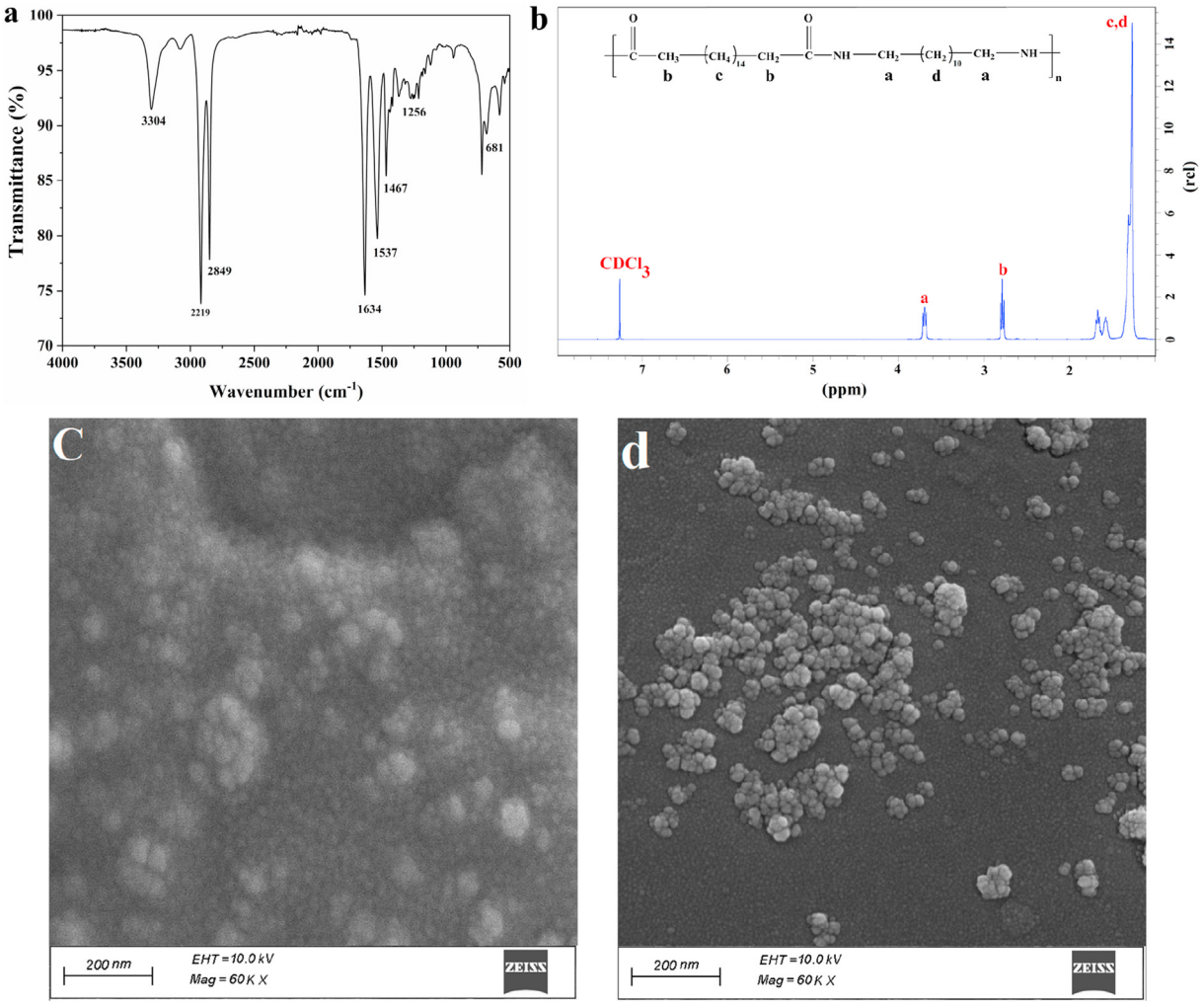

Fig. 2. a) FT-IR and (b) ^{1}H NMR spectra of the synthesized PA1218. (c) SEM image of PA-SSD3 nanocomposite with 60 kx magnification. (d) SEM image of PA-SiO_2 nanocomposite (3 wt%) with 60 kx magnification.

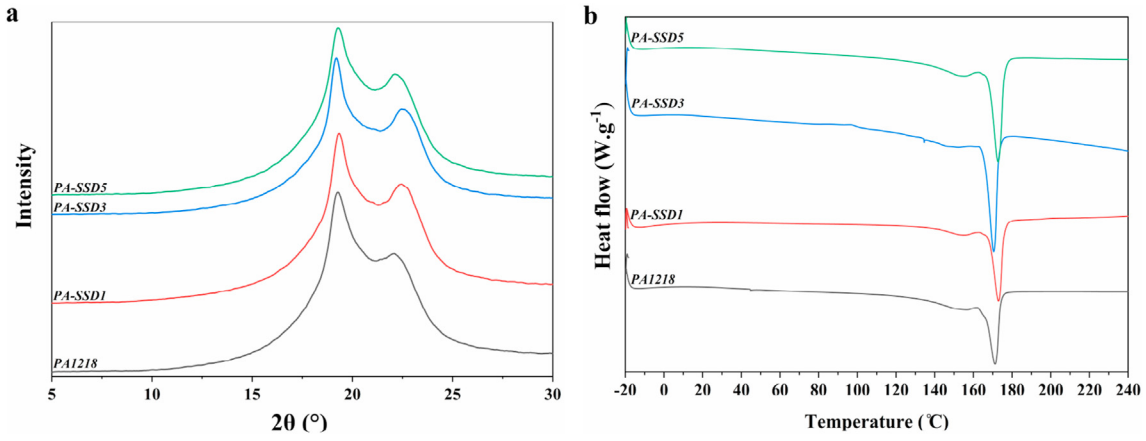

Fig. 3. a) XRD patterns and (b) DSC endothermic thermograms of PA1218 and PA-SSD nanocomposites.

Fig. 3b and Fig. S5 illustrate the second cycle of heating and cooling thermograms, respectively. Furthermore, Table 1 summarizes the relevant parameters, including melting point (T_m), crystallization temperature (Tc), melting enthalpy (ΔH_m), crystallization enthalpy (ΔH_c), and crystallinity (χ_c). All the samples revealed one endothermic peak with a broad shoulder at lower temperature and one exothermic peak, demonstrating that the presence of SSD did not make any new crystal phase, as previously observed in the XRD results. The appearance of the dual melting peaks at approximately 171 °C and 154 °C could be attributed to the melting points of α-

Table 1
DSC results of PA1218 and PA-SSD nanocomposites.

Sample	$T_{m\gamma}$ (°C)	$T_{m\alpha}$ (°C)	T_c (°C)	ΔH_m (kJ/g)	ΔH_c (kJ/g)	χ_c (%)
PA1218	151.64	171.33	146.26	32.262	64.22	11.04
PA-SSD1	153.12	172.79	148.59	36.08	60.01	12.35
PA-SSD3	149.21	170.47	151.03	51.172	55.29	17.51
PA-SSD5	152.80	172.79	148.12	39.65	56.21	13.57

[a] Residual percentage.

and γ-crystalline phases, respectively [24,31]. It is worth noting that the observed melting temperature for PA1218 was relatively lower than that reported for short-chain commercialized PAs such as PA6 (220 °C), PA66 (260 °C), PA11 (191 °C), and PA12 (178 °C) [6]. However, the melting point had good agreement with that reported for PA1216 (171 °C) [33], which has the closest structure to the developed PA1218, as well as with the melting point of PA624 (170 °C) [3], which has the same number of carbon per repeating unit. This relatively lower melting point, which is a notable benefit, could be due to the lower amide linkages per repeat unit and, consequently, a decrease in the number of hydrogen bonds that reduced energy requirements for melting [3,6]. Similarly, the crystallization temperature was significantly lower than that reported for short-chain PAs owing to increased chain flexibility/mobility, higher free volume, and more effective rearrangement of polymer chains [6,31].

Moreover, the SSD nanoparticles did not alter T_m, whereas the crystallization temperature and enthalpy shifted to higher and lower values, respectively, revealing an earlier and accelerated crystallization of the PA1218 phase. In other words, the uniformly dispersed nanoparticles acted as nucleating agents and consequently increased the degree of crystallinity (χ_c) of the matrix [34]. Accordingly, χ_c increased from 11.04 at PA1218 to 17.51% at the PA-SSD3 nanocomposite. However, the crystallinity was reduced at higher SSD content (5%), probably due to nanoparticles' inhomogeneous dispersion into the polymer matrix. It could also be due to the growth of defect crystals, leading to the diminishing of χ_c [35,36]. The similar crystallization behavior has been reported for PA6/silica [24], PA6/graphene oxide [37], and PA12/graphene [34].

3.4. Water absorption results of the synthesized polyamide 1218 and nanocomposites

Table 2 summarizes the water absorption (WA) percentage of the prepared samples. Although the WA of PA1218 (0.51%) was relatively lower than the values reported for PA6 (9.5%) and PA66 (8.53%), it was comparable with the water absorption capacity of PA624 (0.67%), having the same number of carbons per repeating unit [3]. This low water uptake capacity could be attributed to the increased number of non-polar aliphatic groups and the reduced amide linkage density, which originated from hydrogen bonds with water molecules. Furthermore, WA did not change significantly upon increasing the SSD content indicating the incorporation of SSD nanoparticles, and its concentration did not change the primary water diffusion mechanism of PA1218 [38]. This characteristic could be a unique property for the newly developed PA and its nanocomposites regarding material properties, utilization, and storage.

3.5. Static mechanical properties of the synthesized polyamide 1218 and nanocomposites

Fig. 4a provides the stress-strain curves of all the samples. Moreover, Table 2 summarizes the relevant mechanical properties, including tensile modulus, yield strength, tensile strength, elongation at break, and toughness. The tensile modulus and strength of the synthesized PA1218 were significantly higher than those reported for PA624 [3], which has a similar number of carbons per repeating unit. In other words, the tensile modulus and tensile strength were 200% and 35% higher, respectively. However, the elongation at break was 400% lower, indicating a stiffer structure was prepared through polycondensation polymerization between C12-diamine and C18-dicarboxylic acid. Additionally, a slight difference was observed between the humid- and dried-PA1218 mechanical properties due to its relatively low water absorption capacity, as previously observed. This stable mechanical property could be an outstanding characteristic for the developed PA1218 since it is known that the tensile strength and modulus of PA6 decrease in humid conditions, mainly due to the plasticization of water molecules [39].

Furthermore, all the prepared samples' stress-strain curves demonstrated a yield point followed by plastic deformation. They also illustrated strain hardening in which polymer chains orientated from and aligned in the direction of the load caused an increase in the matrix's strength and stiffness in stretch direction, similar to the trend observed for layered-silicate-based nanocomposites [40]. The SSD presence did not significantly affect polymer chains' orientation in the applied force direction due to the favorable interfacial interactions and good compatibility between nanoparticles and PA matrix resulting from surface modification of SSD with OA [41]. In addition, the tensile modulus, yield strength, tensile strength, elongation at break, and toughness, which corresponded to the energy or work required for rupture, were increased notably upon increasing the nanoparticles. In other words, tensile modulus, tensile strength, and elongation at break were increased by 26%, 22%, and 13%, respectively, for the samples containing 3% SSD. It is known that the interfacial bonding between the matrix and nanoparticles and the distribution of nanofillers are two crucial factors influencing the strength, toughness, and elongation of the composite materials [42]. Accordingly, the nanocomposite samples' improved mechanical properties could be attributed to the uniform distribution of nanoparticles into the polymer matrix via the employed *in-situ* polymerization and the strong interfacial adhesion and excellent compatibility between the SSD nanoparticles and the PA1218 matrix obtained through the successfully surface

Table 2
Mechanical properties and water absorption capacity of PA1218 and PA-SSD nanocomposites.

Samples	Tensile modulus (GPa)	Yield strength (MPa)	Tensile strength (MPa)	Elongation at break (%)	Toughness (MPa)	WA (%)
PA1218[a]	1.691 ± 0.050	25.59 ± 1.05	43.47 ± 1.95	106 ± 4	3330 ± 112	–
PA1218	1.664 ± 0.061	25.51 ± 1.10	43.12 ± 1.82	108 ± 4	3387 ± 125	0.51 ± 0.018
PA-SSD1	1.861 ± 0.072	31.24 ± 1.24	47.61 ± 2.17	116 ± 6	3873 ± 164	0.49 ± 0.019
PA-SSD3	2.134 ± 0.092	40.35 ± 1.52	52.78 ± 2.16	120 ± 6	4170 ± 154	0.52 ± 0.02
PA-SSD5	2.283 ± 0.091	30.31 ± 1.20	44.63 ± 1.81	99 ± 4	3407 ± 133	0.48 ± 0.016
PA-SiO2[b]	1.994 ± 0.091	25.46 ± 1.32	27.65 ± 1.41	61 ± 3	1598 ± 71	–

[a] Dried sample.
[b] Nanocomposite with 3 wt% unmodified SiO_2 nanoparticles.

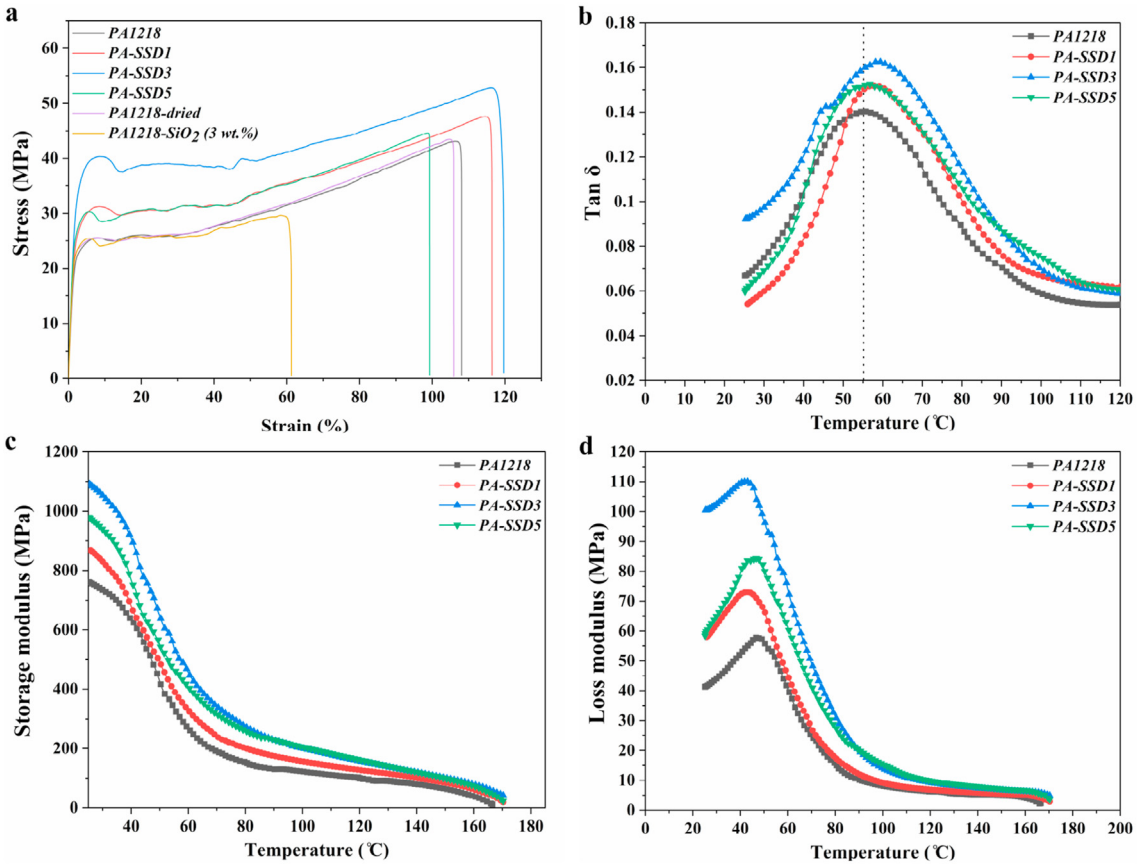

Fig. 4. a) stress-strain curves of PA1218, PA-SDD nanocomposites, and PA-SiO_2 nanocomposite with 3 wt% nanoparticles. (b) tan δ, (c) storage modulus, and (d) loss modulus of PA1218 and PA-SDD nanocomposites versus temperature.

modification of SiO_2 nanoparticles with OA. For supporting the latter, the mechanical properties of the nanocomposite containing 3 wt% untreated SiO_2 nanoparticles were measured. As summarized in Table 2, the yield strength tensile strength, elongation at break, and toughness of this sample were much less than the other samples, which could be due to the heterogeneous dispersion and agglomeration of unmodified SiO_2 nanoparticles in the polymer matrix. It is worth noting that the mechanical properties of the PA-SSD nanocomposites were slightly reduced at 5% loading of SSD, probably owing to the aggregation of nanoparticles into the PA1218 matrix. The similar trend has been reported for PA66/tetraethoxysilane [9,43], PA6/amino-functionalized mesoporous silica nanoparticles [26], and PA6/polysiloxane [44].

3.6. Dynamic mechanical properties of the synthesized polyamide 1218 and nanocomposites

The neat PA1218 and PA-SSD nanocomposites were subjected to DMA in tension mode, and the variation of loss tangent (tan δ), storage modulus (E′), and loss modulus (E″) versus temperature and SSD loading were studied (Fig. 4). The glass transition temperature (T_g) of the neat PA1218 extracted from the tan δ curve (Fig. 4b) was approximately 55 °C. This value was relatively lower than that reported for commercial PA6, PA11, and PA12 and some specific long-chain aliphatic PAs such as PA1010, PA614, and PA618 [6,9]. The increase in the repeating unit length resulted in enhanced flexibility of the main backbone chain and reduced the activation energy required for glass transition [6]. All PA-SSD nanocomposites revealed the elevated T_g compared to the neat PA1218 due to the enhanced interfacial bonding between PA1218 and surface-modified nanoparticles, constraining the chains and segments [45]. Nevertheless, PA-SSD5 illustrated a reduction in the T_g value, which could be due to the increase in the free volume resulting from nanoparticles' aggregation at higher loading [46].

Moreover, the storage modulus of all the samples (Fig. 4c) demonstrated a decreasing trend upon temperature due to the softening and movement of polymer chains and segments at high temperatures. However, it was more pronounced at temperatures between 50 and 100 °C, corresponding to the transitioning from a glassy region to a rubbery state known as glass transition temperature (T_g), as previously observed in the tan δ curve. In addition, the storage and loss moduli (Fig. 4c and d) were relatively higher in all the nanocomposite samples before and after the glass transition, being in agreement with the literature [47,48]. For instance, E′ was 761 MPa for the pure PA1218 at 25 °C, while it was increased to 1090 MPa in PA-SSD3, meaning that more than 40% improvement was achieved by adding 3% SSD nanoparticles. This improvement confirmed the nanoparticles' stiffness effect attributed to the uniform dispersion of the rigid SSD into the PA1218 matrix, as previously observed in the SEM images and tensile test results. Moreover, the observed reduction for PA-SSD5 could be due to the SSD nanoparticles' agglomeration at higher loading.

3.7. Thermal stability of the synthesized polyamide 1218 and nanocomposites

Fig. 5 describes the TGA/DTG curves of PA1218 and PA-SSD nanocomposites, as measured by TGA under nitrogen

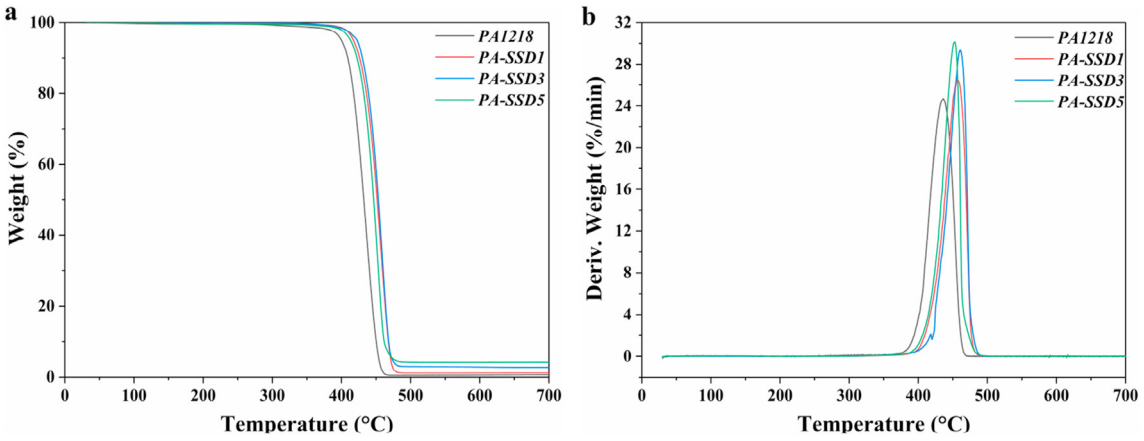

Fig. 5. a) TGA and (b) DTG thermograms of PA1218 and PA-SSD nanocomposites.

atmosphere. Additionally, Table S1 presents the corresponding results, including decomposition temperature at 5% ($T_{5\%}$), 10% ($T_{10\%}$), maximum decomposition temperature (T_{max}), and residual percentage. All samples demonstrated a similar weight loss trend, including a stable mass before 400 °C, followed by a complete decomposition between 400 and 550 °C, being consistent with the literature data [19,49]. Nevertheless, significant differences could be observed between the thermograms of neat PA1218 and PA-SSD nanocomposites. For instance, $T_{5\%}$ and T_{max} were 399.92 and 435.87 °C in PA1218, while they increased to 422.69 and 460.75 °C in the PA-SSD3 nanocomposite. This improvement could be owing to the uniform dispersion of highly thermal resistant SSD nanoparticles and their interactions with the polymer via physical bonding such as electrostatic and steric interactions [43,49]. Both phenomena could restrict the polyamide macromolecular chain movements during heating and improve the matrix's thermal stability. However, after a threshold concentration was exceeded (3%), the sample's thermal stability started to decrease, which might be reasoned based on the aggregation of SSD nanoparticles and their inhomogeneous dispersion in the matrix. It could also be attributed to an inherently weaker structure due to loss in crystallinity, as found in the DSC study [43]. In addition, considering the residue of SSD and pure PA1218 at 700 °C (87.23% and 0.31%, respectively), it could be concluded that the residue left at 700 °C had good agreement with the experimental SSD content. It could be another evidence of the uniform dispersion of the nanoparticles into the polymer matrix achieved via the *in-situ* polymerization [43].

3.8. Rheological properties of the synthesized polyamide 1218 and nanocomposites

Rheological properties of the material at the molten state depend on the structure, size, shape, and dispersion state of nanoparticles [50]. Accordingly, the rheological measurements were performed for all the elaborated samples to further study the degree of the SSD dispersion into the PA1218 matrix. Fig. 6 depicts the frequency-dependence of the storage modulus (G′) and complex viscosity (|η*|). Furthermore, Fig. S6 represents the behavior of the loss modulus (G″) and loss factor, which is the ratio of G″ over G′, as a function of frequency and SSD loading. At the temperature and frequencies employed for the rheological measurements, the PA1218 chains were fully relaxed and exhibited a liquid-like or typical terminal behavior (G' < G″ or loss factor > 1, Fig. S6b) in which the storage modulus is dependent on frequencies [51]. Accordingly, the storage modulus of all the samples was increased upon increasing the frequency. Moreover, G′ and G″ were generally higher in all the nanocomposite samples and were increased with increasing the SSD content due to nanoparticles' stiffening effect resulting from their uniform dispersion into the matrix through the employed *in-situ* polymerization [48,50].

In addition, at lower frequencies, all the samples revealed a Newtonian behavior where the viscosity was independent of frequency (Fig. 6b). However, at higher ones, they demonstrated a non-Newtonian trend in which the viscosity was decreased with the increase in the frequency, being in good agreement with the

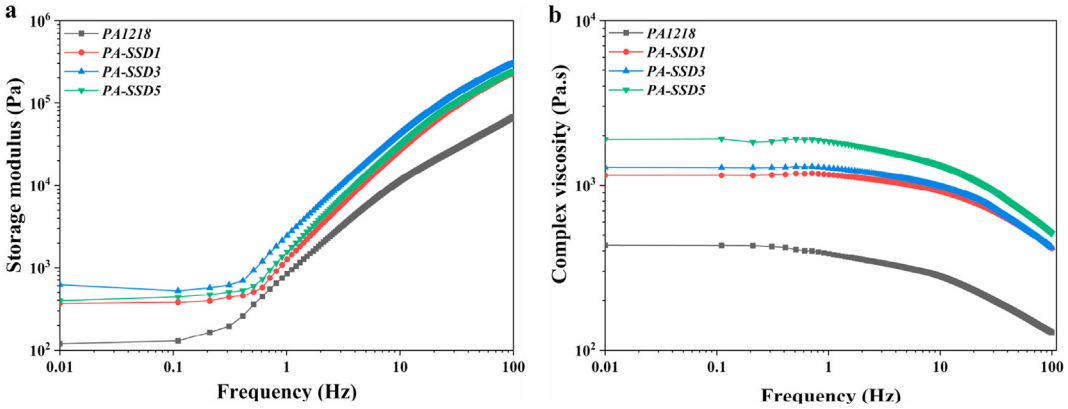

Fig. 6. a) storage modulus and (b) complex viscosity of PA1218 and PA-SSD nanocomposites versus frequency.

scientific literature [52]. In other words, all the samples illustrated a shear-thinning behavior attributed to the lack of time for the polymer chain to respond to the applied oscillation at higher frequencies [48]. Furthermore, the viscosity of PA1218 was increased upon increasing the SSD content, which was attributed to the frictional interaction between SSD nanoparticles and the formation of interconnected physical networks, thereby inducing a reduction in the mobility of PA1218 polymer chains [53].

4. Conclusion

A new kind of long-chain aliphatic polyamide was successfully synthesized via a polycondensation reaction between 1,18-octadecanedioic acid and 1,12-diaminodecane. Compared to commercially available PAs, this newly developed PA1218 revealed a relatively lower melting point and water uptake capacity, along with stable mechanical properties in wet conditions. Furthermore, the positive effect of the addition of surface-modified SiO_2 on the thermomechanical and rheological properties of PA1218 was proved. Overall, the current study findings could introduce this newly developed PA1218 and its nanocomposites with surface-modified SiO_2 nanoparticles as an interesting candidate for numerous engineering applications.

Author statement

Hossein Baniasadi: Conceptualization, Methodology, Formal analysis, Investigation, Writing – original draft, Writing – review & editing, and Visualization, **Jukka Seppälä**; Supervision, Funding acquisition, Writing – review & editing.

Declaration of competing interest

The authors declare that they have no known competing financial interests or personal relationships that could have appeared to influence the work reported in this paper.

Acknowledgment

The authors would like to acknowledge the funding of the Academy of Finland; No. 327248.
(ValueBiomat) and 327865 (Bioeconomy).

Appendix A. Supplementary data

Supplementary data to this article can be found online at https://doi.org/10.1016/j.mtchem.2021.100450.

References

[1] M. Kyulavska, N. Toncheva-Moncheva, J. Rydz, Biobased Polyamide Ecomaterials and Their Susceptibility to Biodegradation, 2017, https://doi.org/10.1007/978-3-319-48281-1_126-1.
[2] S.P. Rwei, P. Ranganathan, W.Y. Chiang, Y.H. Lee, Synthesis and characterization of copolyamides derived from novel aliphatic bio-based diamine, J. Appl. Polym. Sci. 135 (2018) 1–11, https://doi.org/10.1002/app.46878.
[3] P.H. Nguyen, S. Spoljaric, J. Seppälä, Renewable polyamides via thiol-ene 'click' chemistry and long-chain aliphatic segments, Polymer 153 (2018) 183–192, https://doi.org/10.1016/j.polymer.2018.08.033.
[4] R. Ajdary, N. Kretzschmar, H. Baniasadi, J. Trifol, J. Seppälä, J. Partanen, O.J. Rojas, Selective Laser Sintering of Lignin-Based Composites 9, 7th ed., ACS Sustainable Chemistry & Engineering, U.S.A, 2021, pp. 2727–2735.
[5] G. Haddou, A. Roggero, J. Dandurand, E. Dantras, P. Ponteins, C. Lacabanne, Dynamic relaxations in a bio-based polyamide with enhanced mechanical modulus, J. Appl. Polym. Sci. 135 (2018) 2–7, https://doi.org/10.1002/app.46846.
[6] P.H. Nguyen, S. Spoljaric, J. Seppälä, Redefining polyamide property profiles via renewable long-chain aliphatic segments: towards impact resistance and low water absorption, Eur. Polym. J. 109 (2018) 16–25, https://doi.org/10.1016/j.eurpolymj.2018.08.057.
[7] Y.P. Chang, P.B. Cheah, C.C. Seow, Plasticizing-antiplasticizing effects of water on physical properties of tapioca starch films in the glassy state, J. Food Sci. 65 (2000) 445–451, https://doi.org/10.1111/j.1365-2621.2000.tb16025.x.
[8] J. Jiang, Q. Tang, X. Pan, Z. Xi, L. Zhao, W. Yuan, Structure and morphology of thermoplastic polyamide elastomer based on long chain polyamide 1212 and renewable poly(trimethylene glycol), Ind. Eng. Chem. Res. (2020), https://doi.org/10.1021/acs.iecr.0c01334.
[9] M.I. Sarwar, S. Zulfiqar, Z. Ahmad, Polyamide–silica nanocomposites: mechanical, morphological and thermomechanical investigations, Polym. Int. 57 (2008) 292–296.
[10] C. Zhao, P. Zhang, L. Yi, F. Xu, X. Wang, J. Yong, Study on the non-isothermal crystallization kinetics of novel polyamide 6/silica nanocomposites containing epoxy resins, Polym. Test. 27 (2008) 412–419, https://doi.org/10.1016/j.polymertesting.2008.01.001.
[11] W.E. Van Zyl, M. García, B.A.G. Schrauwen, B.J. Kooi, J.T.M. De Hosson, H. Verweij, Hybrid polyamide/silica nanocomposites: synthesis and mechanical testing, Macromol. Mater. Eng. 287 (2002) 106–110, https://doi.org/10.1002/1439-2054(20020201)287:2<106::AID-MAME106>3.0.CO;2-2.
[12] H. Abadikhah, E.N. Kalali, S. Behzadi, S.A. Khan, X. Xu, S. Agathopoulos, Amino functionalized silica nanoparticles incorporated thin film nanocomposite membrane with suppressed aggregation and high desalination performance, Polymer 154 (2018) 200–209, https://doi.org/10.1016/j.polymer.2018.09.007.
[13] H. Abadikhah, E. Naderi Kalali, S. Khodi, X. Xu, S. Agathopoulos, Multifunctional thin-film nanofiltration membrane incorporated with reduced graphene oxide@TiO2@Ag nanocomposites for high desalination performance, dye retention, and antibacterial properties, ACS Appl. Mater. Interfaces 11 (2019) 23535–23545, https://doi.org/10.1021/acsami.9b03557.
[14] M. McCaffrey, H. Hones, J. Cook, R. Krchnavek, W. Xue, Geometric analysis of dielectric failures in polyimide/silicon dioxide nanocomposites, Polym. Eng. Sci. 59 (2019) 1897–1904, https://doi.org/10.1002/pen.25190.
[15] A.M.A. Abdelsamad, A.S.G. Khalil, M. Ulbricht, Influence of controlled functionalization of mesoporous silica nanoparticles as tailored fillers for thin-film nanocomposite membranes on desalination performance, J. Membr. Sci. 563 (2018) 149–161, https://doi.org/10.1016/j.memsci.2018.05.043.
[16] A. Shakeri, R. Razavi, H. Salehi, M. Fallahi, T. Eghbalazar, Thin film nanocomposite forward osmosis membrane embedded with amine-functionalized ordered mesoporous silica, Appl. Surf. Sci. 481 (2019) 811–818, https://doi.org/10.1016/j.apsusc.2019.03.040.
[17] H. Bagheri, A. Roostaie, Electrospun modified silica-polyamide nanocomposite as a novel fiber coating, J. Chromatogr., A 1324 (2014) 11–20, https://doi.org/10.1016/j.chroma.2013.11.024.
[18] R. Pang, K. Zhang, Fabrication of hydrophobic fluorinated silica-polyamide thin film nanocomposite reverse osmosis membranes with dramatically improved salt rejection, J. Colloid Interface Sci. 510 (2018) 127–132, https://doi.org/10.1016/j.jcis.2017.09.062.
[19] P. Theil-Van Nieuwenhuyse, V. Bounor-Legaré, P. Bardollet, P. Cassagnau, A. Michel, L. David, F. Babonneau, G. Camino, Phosphorylated silica/polyamide 6 nanocomposites synthesis by in situ sol-gel method in molten conditions: impact on the fire-retardancy, Polym. Degrad. Stabil. 98 (2013) 2635–2644, https://doi.org/10.1016/j.polymdegradstab.2013.09.027.
[20] T.T. Zhu, C.H. Zhou, F.B. Kabwe, Q.Q. Wu, C.S. Li, J.R. Zhang, Exfoliation of montmorillonite and related properties of clay/polymer nanocomposites, Appl. Clay Sci. 169 (2019) 48–66, https://doi.org/10.1016/j.clay.2018.12.006.
[21] Z. Cherifi, B. Boukoussa, A. Zaoui, M. Belbachir, R. Meghabar, Structural, morphological and thermal properties of nanocomposites poly(GMA)/clay prepared by ultrasound and in-situ polymerization, Ultrason. Sonochem. 48 (2018) 188–198, https://doi.org/10.1016/j.ultsonch.2018.05.027.
[22] Z. Li, Y. Zhu, Surface-modification of SiO_2 nanoparticles with oleic acid, Appl. Surf. Sci. 211 (2003) 315–320, https://doi.org/10.1016/S0169-4332(03)00259-9.
[23] H. Baniasadi, J. Trifol, A. Ranta, J. Seppälä, Exfoliated clay nanocomposites of renewable long-chain aliphatic polyamide through in-situ polymerization, Compos. B Eng. (2021) 108655.
[24] K. Nagel, S. Spange, Polyamide/silica hybrid materials by anionic melt polymerization of lactam-substituted silane monomers with ε-caprolactam, Eur. Polym. J. 113 (2019) 385–394, https://doi.org/10.1016/j.eurpolymj.2019.01.072.
[25] Z. Cai, X. Liu, Q. Zhou, Y. Wang, C. Zhu, X. Xiao, D. Fang, H. Bao, The structure evolution of polyamide 1212 after stretched at different temperatures and its correlation with mechanical properties, Polymer 117 (2017) 249–258, https://doi.org/10.1016/j.polymer.2017.04.037.
[26] H. Gu, Y. Guo, S.Y. Wong, Z. Zhang, X. Ni, Z. Zhang, W. Hou, C. He, V.P.W. Shim, X. Li, Study of amino-functionalized mesoporous silica nanoparticles (NH 2-MSN) and polyamide-6 nanocomposites co-incorporated with NH 2-MSN and organo-montmorillonite, Microporous Mesoporous Mater. 170 (2013) 226–234, https://doi.org/10.1016/j.micromeso.2012.12.010.
[27] H. Wu, B. Tang, P. Wu, Optimizing polyamide thin film composite membrane covalently bonded with modified mesoporous silica nanoparticles, J. Membr. Sci. 428 (2013) 341–348, https://doi.org/10.1016/j.memsci.2012.10.053.
[28] I. Kim, S. Lee, J.G. Kim, G. Park, Analysis of nitrogen recombination activity on silicon dioxide with stagnation heat-transfer, Acta Astronaut. 177 (2020) 386–397, https://doi.org/10.1016/j.actaastro.2020.07.040.

[29] L. Tao, K. Liu, T. Li, R. Xiao, Structure and properties of bio-based polyamide 109 treated with superheated water, Polym. Int. 68 (2019) 1430–1440, https://doi.org/10.1002/pi.5835.
[30] A. Touris, A. Turcios, E. Mintz, S.R. Pulugurtha, P. Thor, M. Jolly, U. Jalgaonkar, Effect of Molecular Weight and Hydration on the Tensile Properties of Polyamide 12, Results Mater (2020) 100149.
[31] S.P. Rwei, P. Ranganathan, Y.H. Lee, Synthesis and characterization of low melting point PA6 copolyamides from ε-caprolactam with bio-based polyamide salt, J. Mol. Struct. 1186 (2019) 285–292, https://doi.org/10.1016/j.molstruc.2019.03.044.
[32] H. Ren, Z. He, J. Xu, X. Yan, P. Liu, Evaluation of the abilities of ozone resistance for polyamide fibers: structures, properties, and aging mechanism, Ind. Eng. Chem. Res. 58 (2019) 17814–17823, https://doi.org/10.1021/acs.iecr.9b03284.
[33] W. Li, D. Yan, Crystal Structure of Novel Polyamides with Long Diacid 2003, 2003, pp. 6–9.
[34] M. Adel, O. El-Shazly, E.W.F. El-Wahidy, A. El-Maghraby, M.A.A. Mohamed, Eco-friendly produced lightweight structural graphene/polyamide 12 nanocomposite: mechanical performance and the controlling microstructural mechanisms, Polym. Eng. Sci. 58 (2018) 1201–1212, https://doi.org/10.1002/pen.24683.
[35] J.P. Jog, Crystallisation in polymer nanocomposites, Mater. Sci. Technol. 22 (2006) 797–806, https://doi.org/10.1179/174328406X101300.
[36] V.P. Cyras, D.A. D'amico, L.B. Manfredi, Crystallization behavior of polymer nanocomposites, in: Cryst. Multiph. Polym. Syst., Elsevier, 2018, pp. 269–311.
[37] C.C.N. de Melo, C.A.G. Beatrice, L.A. Pessan, A.D. de Oliveira, F.M. Machado, Analysis of nonisothermal crystallization kinetics of graphene oxide - reinforced polyamide 6 nanocomposites, Thermochim. Acta 667 (2018) 111–121, https://doi.org/10.1016/j.tca.2018.07.014.
[38] H. Zhao, R.K.Y. Li, Effect of water absorption on the mechanical and dielectric properties of nano-alumina filled epoxy nanocomposites, Composer Part A Appl. Sci. Manuf. 39 (2008) 602–611.
[39] J. Sun, L. Qian, J. Li, Flame retardancy and mechanical properties of polyamide 6 modified by multiple reactions with furan-phosphamide, Polymer (2020) 122994.
[40] A. Mesbah, F. Zaïri, M. Naït-Abdelaziz, J.M. Gloaguen, K. Anoukou, A. Zaoui, Z. Qu, T. Boukharouba, J.M. Lefebvre, Micromechanics-based constitutive modeling of plastic yielding and damage mechanisms in polymer-clay nanocomposites: application to polyamide-6 and polypropylene-based nanocomposites, Compos. Sci. Technol. 101 (2014) 71–78, https://doi.org/10.1016/j.compscitech.2014.05.032.
[41] S.K. Rahimi, J.U. Otaigbe, The effects of the interface on microstructure and rheo-mechanical properties of polyamide 6/cellulose nanocrystal nanocomposites prepared by in-situ ring-opening polymerization and subsequent melt extrusion, Polymer 127 (2017) 269–285, https://doi.org/10.1016/j.polymer.2017.08.064.
[42] W. Jia, J. Wang, L. Ma, S. Ren, S. Yang, Mechanical properties and thermal stability of porous polyimide/hollow mesoporous silica nanoparticles composite films prepared by using polystyrene microspheres as the pore-forming template, J. Appl. Polym. Sci. 137 (2020) 48792.
[43] R. Sengupta, A. Bandyopadhyay, S. Sabharwal, T.K. Chaki, A.K. Bhowmick, Polyamide-6,6/in situ silica hybrid nanocomposites by sol-gel technique: synthesis, characterization and properties, Polymer 46 (2005) 3343–3354, https://doi.org/10.1016/j.polymer.2005.02.104 (Guildf).
[44] S. Fan, B. Peng, R. Yuan, D. Wu, X. Wang, J. Yu, F. Li, A novel Schiff base-containing branched polysiloxane as a self-crosslinking flame retardant for PA6 with low heat release and excellent anti-dripping performance, Compos. B Eng. 183 (2020) 107684.
[45] X. Zhao, Y. Li, W. Chen, S. Li, Y. Zhao, S. Du, Improved fracture toughness of epoxy resin reinforced with polyamide 6/graphene oxide nanocomposites prepared via in situ polymerization, Compos. Sci. Technol. 171 (2019) 180–189.
[46] P. Bandyopadhyay, S. Banerjee, Synthesis, characterization and gas transport properties of polyamide-tethered polyhedral oligomeric silsesquioxane (POSS) nanocomposites, Ind. Eng. Chem. Res. 53 (2014) 18273–18282, https://doi.org/10.1021/ie503475k.
[47] S. Krishna, C.M. Patel, Experimental and computational study of mechanical properties of nylon 6 nanocomposites reinforced with coconut shell nanoparticles, Mater. Today Commun. 24 (2020) 100981.
[48] M.E.M. Mekhzoum, M. Raji, D. Rodrigue, R. Bouhfid, The effect of benzothiazolium surfactant modified montmorillonite content on the properties of polyamide 6 nanocomposites, Appl. Clay Sci. 185 (2020) 105417.
[49] G.L. Jadav, P.S. Singh, Synthesis of novel silica-polyamide nanocomposite membrane with enhanced properties, J. Membr. Sci. 328 (2009) 257–267, https://doi.org/10.1016/j.memsci.2008.12.014.
[50] S. Alix, N. Follain, N. Tenn, B. Alexandre, S. Bourbigot, J. Soulestin, S. Marais, Effect of highly exfoliated and oriented organoclays on the barrier properties of polyamide 6 based nanocomposites, J. Phys. Chem. C 116 (2012) 4937–4947.
[51] L. Shen, Y. Lin, Q. Du, W. Zhong, Y. Yang, Preparation and rheology of polyamide-6/attapulgite nanocomposites and studies on their percolated structure, Polymer 46 (2005) 5758–5766, https://doi.org/10.1016/j.polymer.2005.05.040.
[52] M. Abdelwahab, A. Codou, A. Anstey, A.K. Mohanty, M. Misra, Studies on the dimensional stability and mechanical properties of nanobiocomposites from polyamide 6-filled with biocarbon and nanoclay hybrid systems, Composer Part A Appl. Sci. Manuf. 129 (2020) 105695.
[53] M.B. Mahmud, A. Anstey, V. Shaayegan, P.C. Lee, C.B. Park, Enhancing the mechanical performance of PA6 based composites by altering their crystallization and rheological behavior via in-situ generated PPS nanofibrils, Compos. B Eng. (2020) 108067.